Sensors & Actuators: B. Chemical 350 (2022) 130807

Contents lists available at ScienceDirect

Sensors and Actuators: B. Chemical

journal homepage: www.elsevier.com/locate/snb

Gas sensor based on cobalt-doped 3D inverse opal SnO_2 for air quality monitoring

Ke Chen [a], Yue Zhou [a], Rongrong Jin [a], Tianshuang Wang [b,*], Fangmeng Liu [a], Chenguang Wang [a], Xu Yan [a], Peng Sun [a,*], Geyu Lu [a]

[a] State Key Laboratory of Integrated Optoelectronics, College of Electronic Science and Engineering, Jilin University, 2699 Qianjin Street, Changchun 130012, PR China
[b] State Key Laboratory of Inorganic Synthesis and Preparative Chemistry, College of Chemistry, Jilin University, 2699 Qianjin Street, Changchun 130012, PR China

ARTICLE INFO

Keywords:
Gas sensor
Co-doped SnO_2
Inverse opal structure
VOCs
Dual functionality

ABSTRACT

In this research, a semiconductor metal oxide (SMO)-based gas sensor was designed for the ultrasensitive and tunably selective detection of formaldehyde and acetone. Cobalt-doped 3D inverse opal SnO_2 multilayer films (3D IO Co-SnO_2 MFs) used as sensing materials were prepared with the ultrasonic nebulizing deposition (UND) method combined with a self-assembly template. The 3D IO Co-SnO_2 (Co/Sn = 1:24 atom%) MF-based sensor exhibited a much higher response and lower limit of detection to the volatile organic compounds (VOC) gases because of the larger specific surface area, effective gas accessibility, high catalytic activity, and increased chemisorbed oxygen species generated by the elevation of the Fermi level and the narrowing of the band gap. More importantly, the 3D IO Co-SnO_2 MF-based sensor showed dual-model gas sensing characteristics for selectively detecting formaldehyde and acetone at 200 °C and 225 °C, respectively, because of the difference of the VOC catalytic conversion and surface oxidative reaction rate that was dependent on the operating temperature.

1. Introduction

According to data from the World Health Organization, millions of people die per year due to indoor air pollution, which is highly toxic and ubiquitous, especially for young children who are more easily susceptible to indoor air pollutants compared with adults. The most representative indoor air pollutants are VOCs. Among the VOCs, formaldehyde, as a common harmful VOC, ranks second on the priority control list of toxic chemical substances. Additionally, higher concentration of acetone can cause an anesthetic effect, especially on the nervous system [1–3]. Accordingly, monitoring indoor VOCs is particularly essential. Recently, SMO-based gas sensors with various characteristics, all solid state, miniaturization, and easy integration have become a research hotspot. However, the unavoidable drawbacks of lower sensitivity to trace level VOCs and the poor selectivity of SMO-based gas sensors severely limit applications in exact VOC detection.

To date, some research groups have demonstrated that the design of sensing material nanostructures and in-situ doping can improve the sensing performances of SMO-based gas sensors. The design and preparation of SMO sensing materials with diverse 1D-3D architectures, such as nanowires, nanosheets, and hierarchical nanostructures, have been considered to provide sensing active sites to enhance chemisorbed oxygen species, and the structural design of sensing materials has led to the improvement of gas sensitivity [4–6]. Three-dimensional inverse opal (3D IO) structured materials possess good permeability and porosity, as well as large specific areas and pore volumes that can promote the diffusion of gas molecules and improve thermal stability, and the 3D IO structure has become the most preferred framework [7,8]. Thus, various synthetic strategies have been found to prepare 3D IO sensing materials, such as traditional and simple methods of gravity sedimentation, and the rapid approach of spin coating [9,10]. However, owing to the long processing time, tedious preparation, and the fact that the self-assembled ordered structure can be easily damaged, the above synthetic strategies are not conducive to scale production. The easily achieved and effective approach of ultrasonic nebulizing deposition (UND) has been utilized to prepare 3D IO SMO sensing material, which was first pointed out in our previous report [11]. In addition, the in-situ doping further obviously contributed to the selective detection of trace-level specific VOC gases. This was because the transition metal ion dopants could be used as a catalyst to improve gas sensing reaction

* Corresponding authors.
E-mail addresses: wangtianshuang@jlu.edu.cn (T. Wang), pengsun@jlu.edu.cn (P. Sun).

https://doi.org/10.1016/j.snb.2021.130807
Received 23 April 2021; Received in revised form 19 September 2021; Accepted 21 September 2021
Available online 28 September 2021

activity, and the chemisorbed oxygen generated by the production of oxygen vacancy sites via doping was obviously enhanced [12]. In-situ doping can also lead to the regulation of the nanoparticle crystallite size and affect the intergranular contact, therefore resulting in the baseline resistance change of the SMO-based gas sensor [13–15]. Furthermore, some research articles have demonstrated that the Fermi level position, the electron depleted region width, and the band gap can be regulated by in-situ doping, leading to the control of SMO sensing material conductivity and the concentration of chemisorbed oxygen, and finally the enhancement of the sensitivity and change selectivity [11,16,17]. Although the selective detection of one specific VOC gases using a single high-performance sensor can be achieved with the mentioned strategies, an increase in the number of sensors is inevitable when detecting various indoor VOC gases. From this perspective, the best choice is to develop a single sensor with dual or multiple functions that can exhibit tunable selectivity to build an air quality monitoring system with a minimal number of sensors. Some research groups have reported the application of a gas sensing measurement system in distinguishing VOC gases [18]. However, to the best of our knowledge, there are few reports of one single sensor with a dual-mode sensing characteristic being used in selectively detecting two kinds of specific VOC gases [19–24]. For example, Xu, et al. reported that a PdAu bimetal decorated SnO_2-based gas sensor could exhibit tunable selectivity through the change of the operating temperature [24]. In this research, the doping of heteroatoms and the regulation of a sensing material's microstructure made the SMO-based gas sensor capable of dual-model gas sensing characteristics for the selective detection of formaldehyde and acetone. Table S1 displays a comparison of the other decorated SnO_2-based gas sensors' sensing characteristics (operating temperature, gas response, response and recovery times, and limit of detection) with the sensor in this work. Compared with the reported formaldehyde sensors, it could be highlighted that the 3D IO Co-SnO_2 (1:24 atom%) MF-based sensor exhibited a much higher response, faster response time, and lower limit of detection (50 ppb) to formaldehyde. Additionally, compared with the reported acetone sensors, this sensor exhibited excellent performance, reacted relatively quickly at 225 °C, and possessed the lowest limit of detection (500 ppb) to acetone. However, the sensor with a tunable selectivity showed dual-mode gas sensing characteristics for selectively detecting formaldehyde and acetone at 200 °C and 225 °C, respectively.

In this research, ultrasonic nebulizing deposition (UND) combined with the self-assembly polystyrene spheres (diameter: ~200 nm) template as a new-generation strategy was proposed to synthesize 3D IO Co-SnO_2 MFs. There was a significant increase in specific surface area of the sensing materials and the diffusion rate of gas molecules by employing a 3D IO nanostructure. Compared with the 3D IO SnO_2 MF-based sensor, the 3D IO Co-SnO_2 (1:24 atom%) MF-based sensor exhibited much a higher response, a trace-level limit of detection (50 ppb formaldehyde and 500 ppb acetone), and tunable selectivity. In detail, the 3D IO Co-SnO_2 (1:24 atom%) MFs showed dual-mode gas sensing characteristics for the selective detection of formaldehyde and acetone at 200 °C and 225 °C, respectively. Thus, the dual-mode monitoring of formaldehyde and acetone was achieved by altering the operating temperature. Additionally, according to the characterizations of UV–vis spectrophotometer, ultraviolet photoelectron spectroscopy (UPS), and HCHO temperature programmed spectroscopy (HCHO-TPR), the doping of cobalt could decrease the band gap, elevate the Fermi level position, induce vacancy defects, and increase the surface chemisorbed oxygen, finally resulting in the enhancement of the sensing performance.

2. Experiment

2.1. Synthesis of sensing materials

The 3D IO Co-SnO_2 MF sensing material was synthesized with the ultrasonic nebulization deposition (UND) method combined with the self-assembly PS sphere template (diameter: ~200 nm, Fig. S1). The synthetic path was illustrated in Fig. 1. First, for the precursor solution, certain amounts of $Co(NO_3)_2{\cdot}6H_2O$ (AR, SCR Co. Ltd, China), $SnCl_4{\cdot}5H_2O$ (AR, SCR Co. Ltd, China) (Co/Sn = 1:16, 1:24, and 1:48 atom%), and well-dispersed PS sphere powder was dissolved in a certain volume of the solution containing deionized water, hydrochloric acid solution (38%, SCR Co. Ltd, China) and hydrogen peroxide solution (30%, SCR Co. Ltd, China). Subsequently, the solution was stirred at room temperature for one hour. Second, it was time for ultrasonic nebulizing deposition (UND) (the ultrasonic vibrator frequency = 1.7 MHz) with the nitrogen (flow rate = 1000 sccm) working as the carrier gas. After adding the solvent to the UND system chamber and atomizing for two hours, the precursor slurry of the as-prepared 3D IO Co-SnO_2 MFs was obtained. Finally, the slurry mentioned above was dried at 60 °C for 24 h and annealed at 600 °C for 3 h to prepare the 3D IO Co-SnO_2 MFs powder. In addition, the 3D IO SnO_2 MF sensing material without doping as a control experiment was synthesized with this method to spray the solution and subsequent annealing.

2.2. Fabrication and measurement of gas sensor

The fabricating and gas sensing measurement procedures of the gas sensors are described below (Fig. S2) [25]. The slurry of sensing material powders mixed with ethanol solvent was uniformly coated on the ceramic tube (two thin gold electrodes wrapped around, four platinum wires hanging on, and a Ni-Cr alloy coil passed through as a heater) and annealed at 250 °C for 2 h. Subsequently, the ceramic tube with sensing material was welded onto a hexagon socket. The gas sensor was prepared and aged at 200 °C for 5 days. The gas sensing performance was evaluated by a static test system. First, the gas sensor was put into a sealed chamber filled with clean air (80% N_2 and 20% O_2). The stable value of the gas sensor resistance was labeled as the baseline resistance in air (R_{air}). Subsequently, the gas sensor was transferred into another sealed chamber filled with a mixture of clean air and a certain concentration of target gas. The stable resistance in the target gas was labeled as R_{gas}. Afterwards, the gas sensor was placed back into the sealed chamber with clean air, and the resistance recovered to the baseline resistance (R_{air}). The different concentrations of the target gas were prepared by mixing the standard gas with the target gas, which could be calculated with Eq. (1):

$$C = V_s \times C_s / V, \tag{1}$$

where C: the concentration of the target gas, in ppm, V_s: the volume of standard gas that was injected into the chamber, C_s: the concentration of standard gas (100 ppm standard gas mixing with clean air (80% N_2 and 20% O_2)), V: the volume of the sealed chamber (1 L).

The gas sensor devices were connected to the sensing system and measured by Fluke 8846a (Fluke Co.) to detect the resistance variation in real time. The different heating currents were supplied by the constant-current power (Gwinstek GPD-3303S) to provide energy to the sensor component. The sensitivity was defined as shown in Eq. (2):

$$S = R_{air} / R_{gas}, \tag{2}$$

where R_{air}: the baseline resistance in air and R_{gas}: the resistance in the target gas.

The response time of the SMO gas sensor was defined as the time taken for the original resistance to reach 90% of its resistance at equilibrium reacting in the target gas, while the recovery time was the opposite.

2.3. Characterization methods

The crystal phases of the mentioned samples were characterized by X-ray diffraction (XRD) analysis with a Rigaku wide-angle X-ray diffractometer (D/max 2500) using Cu Kα radiation with a wavelength

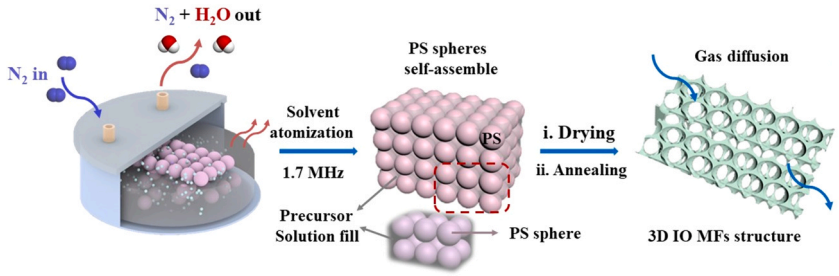

Fig. 1. Illustration of the process flow to fabricate the 3D IO SnO_2 and Co-SnO_2 (Co/Sn = 1:16, 1:24, and 1:48 atom%) MFs.

of 0.154 nm at a scanning rate of five degrees per minute in the range of 20–80 degrees. The characteristic microscopic morphology and the microstructure of the Co-SnO_2 MF sensing samples were observed with field emission scanning electron microscopy (FESEM, JSM-7500F JEOL) and transmission electron microscopy (TEM, JSM-2100F). Energy dispersive X-ray spectroscopy (EDS) attached to the TEM was applied to further investigate the micro-composition. The specific surface area and aperture distribution analysis were measured with Brunauer-Emmet-Teller (BET) through N_2 adsorption-desorption isotherms (Micrometrics Gemini VII). The X-ray photoelectron spectrometer (XPS) measurement was conducted with an ESCALAB 250 X-ray photoelectron spectrometer using an X-ray source (Al Kα hν = 1486.6 eV) to obtain the structural parameters. The work function was calculated according to ultraviolet photoelectron spectroscopy (UPS) tested with the ESCALAB 250 X-ray photoelectron spectrometer. The UPS spectrum used He I (hν = 21.22 eV) as an energy source. The ultraviolet-visible spectrophotometer (UV-2550, Shimadzu, Japan) was applied to obtain the UV visible absorption spectrogram. The HCHO temperature programmed reduction (HCHO-TPR, AMI-300, USA) was measured to characterize the surface redox activity of the materials via a gas analysis mass spectrometer (Omnistar, Pfeiffer, Germany).

3. Results and discussion

3.1. Structural and morphological characterization

The XRD patterns of the synthesized materials of pure SnO_2 and Co-SnO_2 (Co/Sn = 1:16, 1:24, and 1:48 atom%) are shown in Fig. 2(a). All the diffraction peaks matched with the tetragonal rutile structure of SnO_2 (JCPDS 41-1445). There were not any detectable diffraction peaks of cobalt oxide due to the low doping concentration. Additionally, with the increase of the Co doping concentration, the (110) peaks (from 24 to 30 degrees) became broader and shifted to the larger angle side because of the different diameters of Sn^{4+}, Co^{2+}, and Co^{3+}. Because the diameter of cobalt (0.66 Å, average oxidation state of < 3) was smaller than that of tetravalent tin (0.69 Å), the lattice distortion existed when the cobalt ions were doped into the SnO_2 lattice. The Debye-Scherrer formula is as follows (Eq. (3)):

$$D = \frac{0.89\lambda}{\beta\cos\theta}, \tag{3}$$

where $\lambda = 0.154nm$ is the wavelength of the X-ray, β is the half-peak

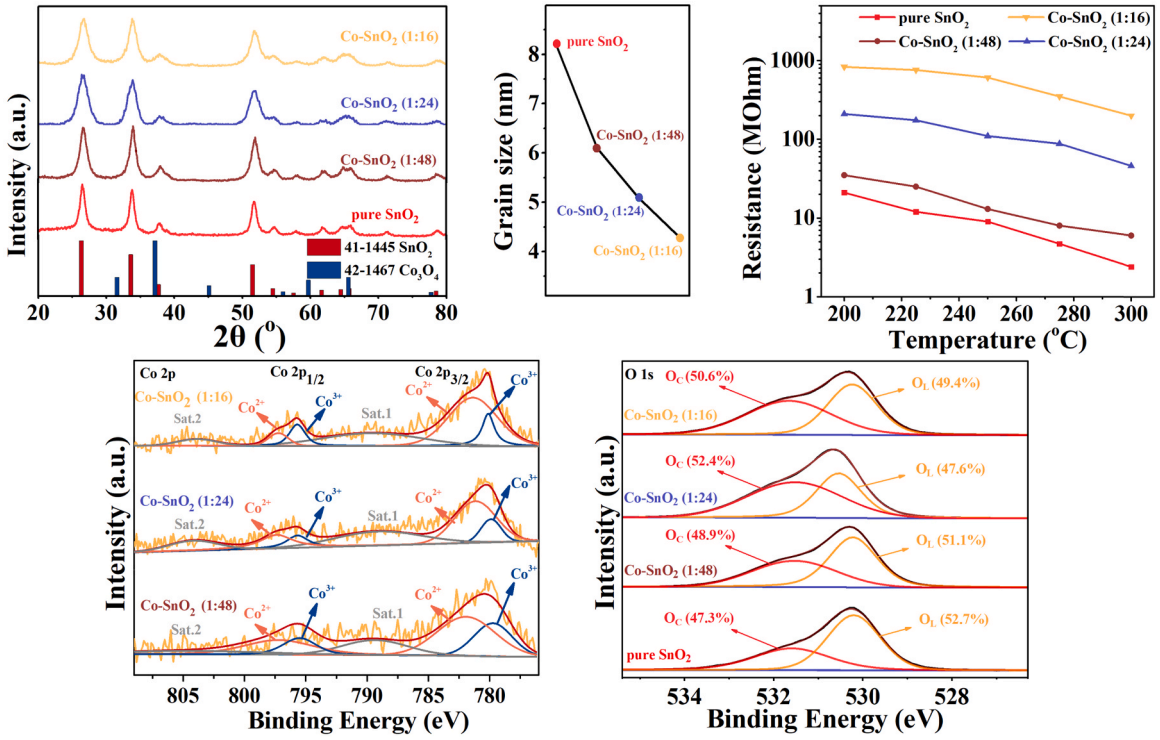

Fig. 2. (a) The XRD patterns of the 3D IO SnO_2 and Co-SnO_2 (Co/Sn = 1:16, 1:24, and 1:48 atom%) MF sensing materials. (b) Different doping concentrations corresponding to various crystallite sizes obtained from XRD analysis. (c) The baseline resistances in air of the 3D IO SnO_2 and Co-SnO_2 (Co/Sn = 1:16, 1:24, and 1:48 atom%) MF-based sensors at different operating temperatures. (d) Co XPS spectra of Co-SnO_2 (Co/Sn = 1:16, 1:24, and 1:48 atom%) MF sensing materials. (e) O XPS spectra of four sensing materials.

breadth, and θ is the Bragg diffraction angle [26]. The average size of crystallites of the pure SnO_2 and Co-SnO_2 (Co/Sn = 1:16, 1:24, and 1:48 atom%) were estimated to be 4.3 nm, 5.0 nm, 6.1 nm, and 8.1 nm (Fig. 2(b)). The incorporation of Co effectively inhibited the grain growth of the SnO_2 and regulated the crystallite size. The crystallite size of the sensing materials gradually decreased with the increase of the doping concentration of cobalt, indicating that the cobalt was successfully doped into SnO_2 lattice, and this resulted in the effective restraint of the SnO_2 grain growth. Furthermore, it was proven that the sensitivity was significantly increased when the crystallite size of the sensing materials was comparable to or smaller than the Debye length [27]. As shown in Fig. 2(c), it could be found that the baseline resistances in air of the Co-SnO_2-based sensors were higher than that of the pure SnO_2-based sensor, and these resistances were gradually enhanced with the increasing doping concentration of the cobalt. The electrons encountered more grain barriers when the electron transfer occurred as the crystallite size became smaller, which showed an increase in resistivity, macroscopically. The heteroion doping could lead to the regulation of the crystallite size and affect the intergranular contact, finally resulting in the baseline resistance change of the SMO-based gas sensor. The XPS analysis was conducted as shown in Fig. 2(d and e). The full spectra XPS of the 3D IO SnO_2 and Co-SnO_2 (Co/Sn = 1:16, 1:24, and 1:48 atom%) MF sensing materials are displayed in Fig. S3. As shown in Fig. 2(d), two peaks were located at 779.9 eV and 795.5 eV, corresponding to the Co $2p_{3/2}$ and Co $2p_{1/2}$. The two Co peaks were divided into Co^{3+} and Co^{2+}, respectively. The $[Co^{3+}]/[Co^{2+}]$ ratios of the Co-SnO_2 (Co/Sn = 1:16, 1:24, and 1:48 atom%) MFs were calculated to be about 0.3, 0.34, and 0.56, and the value of the $[Co^{3+}]/[Co^{2+}]$ ratio decreased with the increased doping concentration [28,29]. The O XPS spectra could be fitted into two peaks: the chemisorbed oxygen (O_C) and the lattice oxygen (O_L) species in Fig. 2(e), located at 531.4 ± 0.2 eV and 530.2 ± 0.2 eV via the Gauss-Lorentz function [30]. The O_L was a relatively stable oxygen species in the crystal lattice and it had no contribution to the electron transfer in the gas sensing reaction. However, the O_C was essential for the gas sensing performance. More chemisorbed oxygen could participate in the reactions with targeted gas molecules on the surface when the O_C species increased. Thus, the sensing materials showed a higher sensitivity. The concentrations of the chemisorbed oxygen species of SnO_2 and Co-SnO_2 (Co/Sn = 1:16, 1:24, and 1:48 atom%) were 47.3%, 50.6%, 52.4%, and 48.9%. Accordingly, the 3D IO Co-SnO_2 (1:24 atom%) MF-based sensor possessed a much higher response that could be attributed to the highest concentration of chemisorbed oxygen species on the sensing material surface.

The scanning electron microscopy (SEM) images of the pure SnO_2 and Co-SnO_2 MFs are shown in Fig. 3(a and b) and Fig. S4. The long-range ordered macroporous structure was constructed using the self-assembly PS sphere template. The spherical pore size was approximately 155–170 nm, which was slightly smaller than the diameter of the PS sphere (average size: ~200 nm) because of the shrinkage of spheres during annealing [31]. Additionally, the 3D macroporous structure of the Co-SnO_2 did not change with the increased amount of dopant. According to the UND preparation process, the specific porous structure of the sensing materials was composed of many stacked nanoparticles after removing the self-assembly PS sphere template through annealing, forming a 3D IO macroporous gas diffusion channel. As shown in Fig. 3(c and d), the macroporous Co-SnO_2 (1:24 atom%) MFs was uniform and continuous. It could be inferred that the nanoparticles wrapped around the surface of the PS spheres and subsequently formed an interconnection between each sphere while self-assembling. To further demonstrate the existence and distribution of the cobalt element in Co-SnO_2, the EDS elemental mappings for the Sn, Co, and O of the Co-SnO_2 sample were conducted, as shown in Fig. 3(d). These three compositions were uniformly distributed and a few cobalt dopants were homogeneously distributed in the SnO_2.

3.2. Sensing properties

The gas sensitivities of the 3D IO pure SnO_2 and Co-SnO_2 MF-based sensors to the 100 ppm target gases (ethanol, formaldehyde, acetone, methanol, benzene, toluene, CO, NO_2) at the temperature range from 200 °C to 300 °C are exhibited in Fig. 4(a-d). It could be found that the 3D IO Co-SnO_2 (Co/Sn = 1:16, 1:24, 1:48 atom%) MF-based sensors all possessed higher sensitivity to 100 ppm formaldehyde at 200 °C compared with the pure SnO_2 MF-based sensor at 225 °C. The 3D IO Co-SnO_2 MF-based sensor with the Co/Sn atom ratio of 1:24 exhibited the highest formaldehyde response of 52.3 among different Co-SnO_2 (Co/Sn

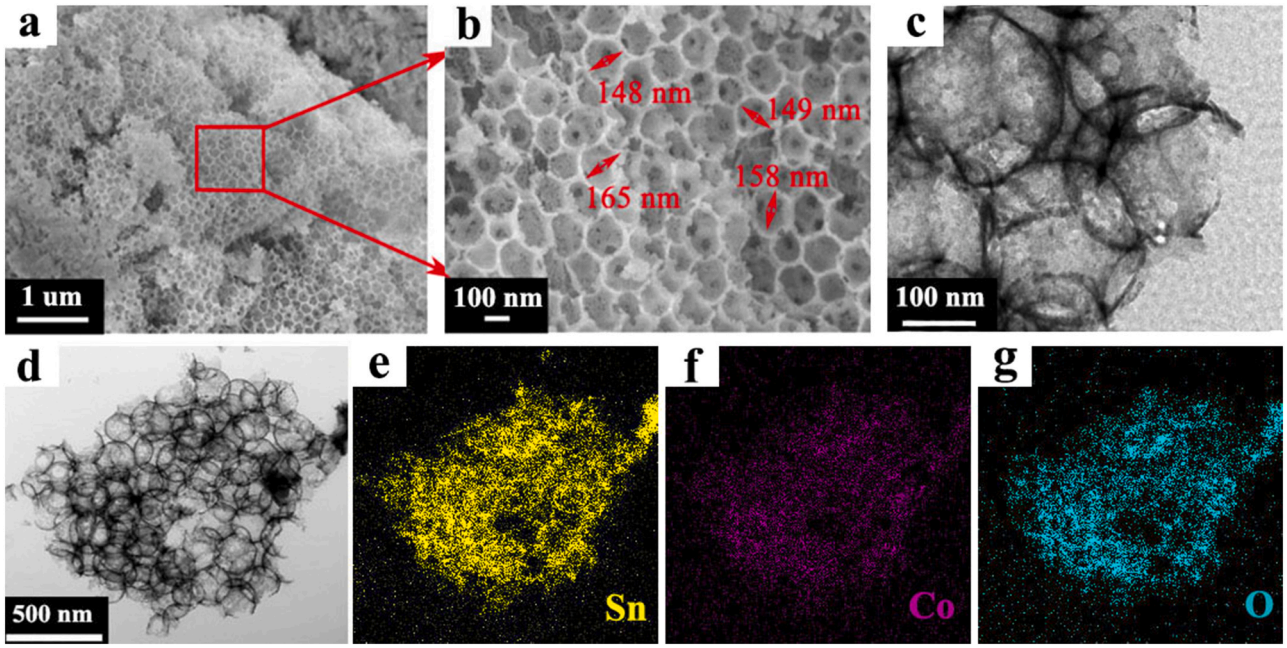

Fig. 3. (a) The SEM image of the 3D IO Co-SnO_2 (1:24 atom%) MF sensing material at a low magnification. (b) The SEM image at a high magnification. (c) The TEM image of the 3D IO Co-SnO_2 (1:24 atom%) MF sensing material at a high magnification. (d) The TEM image at a low magnification and (e, f) the EDS mapping of the Sn, Co, and O elements.

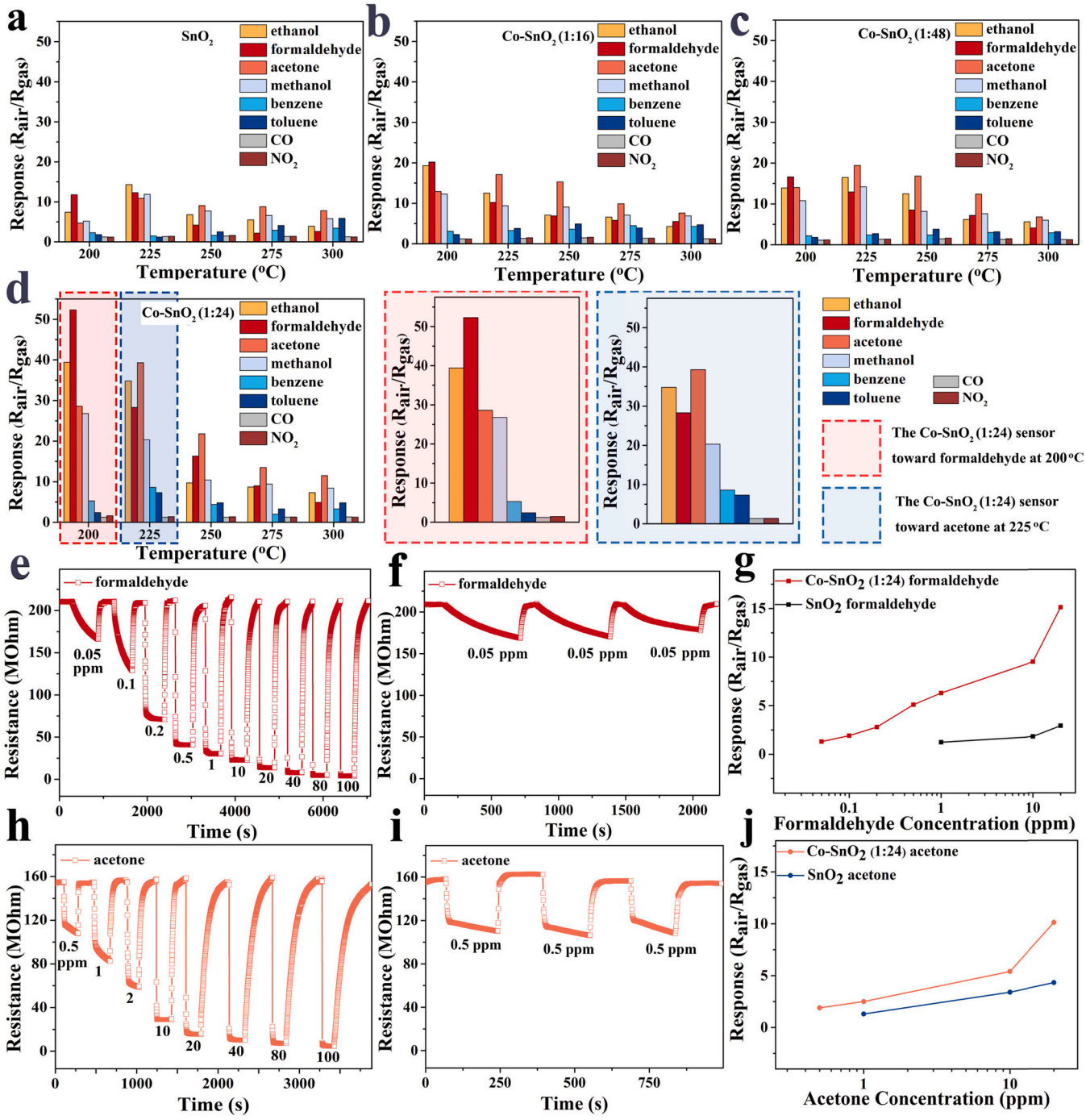

Fig. 4. (a-d) The gas sensitivities of the 3D IO SnO_2 and Co-SnO_2 (Co/Sn = 1:16, 1:24, and 1:48 atom%) MF-based sensors at the temperature range from 200 °C to 300 °C reacting with eight 100 ppm target gases: ethanol, formaldehyde, acetone, methanol, benzene, toluene, CO, and NO_2. The 3D IO Co-SnO_2 (1:24 atom%) MF-based sensor: (e) the dynamic sensing performance for different concentrations of formaldehyde at 200 °C, (f) the resistance change to 0.05 ppm formaldehyde at 200 °C. (g) The sensitivity of the 3D IO SnO_2 and 3D IO Co-SnO_2 (1:24 atom%) MF-based sensor to various concentrations of formaldehyde at the optimized operating temperature. The 3D IO Co-SnO_2 (1:24 atom%) MF-based sensor: (h) the dynamic sensing performance to different concentrations of acetone at 225 °C, (i) the resistance change to 0.5 ppm acetone at 225 °C. (j) The sensitivity of the 3D IO SnO_2 and 3D IO Co-SnO_2 (1:24 atom%) MF-based sensor to various concentrations of acetone at 225 °C.

= 1:16, 1:48 atom%)-based sensors, which was 4.3-times higher than that of pure SnO_2 at the optimal operating temperature. The Co-SnO_2 (1:24 atom%)-based sensor also exhibited the lowest formaldehyde limit of detection of 50 ppb with the response of 1.3 (Fig. 4(e and f)). More importantly, the gas selectivity of the Co-SnO_2 (1:24 atom%)-based sensor could be changed by alternating the operating temperature. The 3D IO Co-SnO_2 (1:24 atom%) MF-based sensor exhibited a superior acetone sensing performance. For example, the response to 100 ppm acetone was 39.8 at 225 °C, which was higher than that of pure SnO_2 (the 100 ppm acetone response was 10.9). As shown in Fig. 4(h and i), the Co-SnO_2 (1:24 atom%)-based sensor could detect a lower concentration (0.5 ppm) of acetone with the response of 1.2. Thus, it was noted that the 3D IO Co-SnO_2 (1:24 atom%) MF-based sensor exhibited a highly selective detection of formaldehyde and acetone at the operating

temperatures of 200 °C and 225 °C (Fig. 4(a-d)), respectively. This demonstrated the promising potential of a single sensor with two different functionalities. Namely, if a very small Co-SnO_2 (1:24 atom %)-based sensor is made on a microheater platform and two different pulse-driven heaters are applied, the gas sensing characteristics at two kinds of operating temperatures can be measured quickly using one sensor, which will facilitate the dual function of a sensor to detect formaldehyde and acetone in a highly selective and sensitive manner.

In this experiment, the selectivity variation could be attributed to the following aspects. The appearance energy was the minimum energy that had to be supplied to a gas phase atom or molecule to produce an ion, and the appearance energy of formaldehyde was smaller than that of acetone. The HCHO deprotonation to the $[CHO]^+$ appearance energy was 11.97 eV, which was lower than the deprotonation of C_3H_5OH to $[C_3H_5O]^+$, measured at 13.10 eV [32]. Thus, the redox reaction between the formaldehyde and O^- could be achieved at a lower thermal energy, and the Co-SnO_2-based sensor exhibited high selectivity to 100 ppm formaldehyde at 200 °C. However, once the operating temperature exceeded 200 °C, desorption could easily occur for the adsorbed formaldehyde molecules before the reaction, so the sensitivity changed [33]. Accordingly, the operating temperature was an essential factor for the gas sensor, and because of the different affinity energy of the gas molecules, the activity of the gas was different at various temperatures. The lowest unoccupied molecular orbital (LUMO) of acetone is lower than that of formaldehyde [34]. When the temperature was above 225 °C, the gas sensing materials were more inclined to react with acetone, leading to the selectivity variation at different temperatures. Therefore, the in-situ selection of the formaldehyde and acetone gas sensor could be realized by changing the operating temperature.

As shown in Fig. 4(g and j), the 3D IO Co-SnO_2 (1:24 atom%)-based sensor exhibited a lower limit of detection than the pure SnO_2-based sensors. The response of both sensors gradually enhanced with the increase of the concentration of the target gas and showed a good linear characteristic curve. Additionally, the response and recovery times of the sensor for the 100 ppm target gas at the respective optimal operating temperatures could be obtained, as shown in Fig. S5. The response times of the Co-SnO_2 (1:24 atom%)-based sensor to the 100 ppm formaldehyde and acetone were all 1 s, indicating that the 3D IO structure was beneficial for the improvement of the gas molecule transportation. The recovery time of the sensor for formaldehyde was within 176 s, but the recovery time of the sensor for acetone was 256 s, which was attributed to the desorption of formaldehyde and acetone gases being relatively slow at the operating temperature [35]. Humidity interference with the sensing properties had to be considered. The water molecules would occupy most active sites on the surface of the sensitive materials at high humidity atmosphere and prevent the sensing reaction between target gas and chemisorbed oxygen, and also inhibit the transformation of the adsorption of oxygen into O^{2-} Thus, higher humidity had a negative impact on the gas sensor. As shown in Fig. 5(a and b), the gas responses of the sensor to formaldehyde at 200 °C and acetone at 225 °C had been decreased in the acceptable ranges while the humidity increasing from 30% RH to 50% RH. Moreover, the gas resistances of the sensor to formaldehyde at 200 °C and acetone at 225 °C were both reduced by about 10% at 30–50% RH, respectively. Besides, the ratio of changes in resistance were lower than the gas response value ($R_{air}/R_{gas} = 1.2$) defined as the detection limit of target gas.

The cyclic performances of the 3D IO Co-SnO_2 (1:24 atom%) MF-based sensor for 100 ppm formaldehyde and acetone were measured at 200 °C and 225 °C, respectively (Fig. S6). The sensor could return to baseline resistance each time after detecting the target gases, and the sensor possessed extraordinary reliability and repeatability, even after repetitive measurements. For the long-term stability measurement (Fig. 5(c and d)), the response of the 3D IO Co-SnO_2 (1:24 atom%) MF-based sensor to formaldehyde and acetone and the baseline resistance (~195 MΩ at 200 °C and ~140 MΩ at 225 °C) were steady, indicating that the sensor could remain relatively stable after long-term stability measurement at the optimal operating temperature for 12 days.

Thus, the 3D IO Co-SnO_2 (1:24 atom%) MF-based sensor exhibited excellent sensing performance toward formaldehyde and acetone with the in-situ altering operating temperature for dual-mode sensing characteristics.

3.3. Gas sensing mechanism

The sensing performance of SMO gas sensors to VOC gas is associated with the surface chemisorbed oxygen, and the surface chemisorbed oxygen species is O^- at the temperature of 150–400 °C (Eq. (4)) [36,37]. The sensing mechanism is briefly described as follows: (i) At step one, when the SnO_2 is exposed to air, because the electron affinity of an oxygen molecule is higher than the work function of the SnO_2, the electron will be captured by oxygen, thus leading to the existence of a chemisorbed oxygen ion.

$$O_2(ads) + 2e^- \leftrightarrow 2O^-(ads) \quad (4)$$

Simultaneously, the transfer of the electron induced the band to bend upward and form the electron depletion layer, which causes the SMO gas

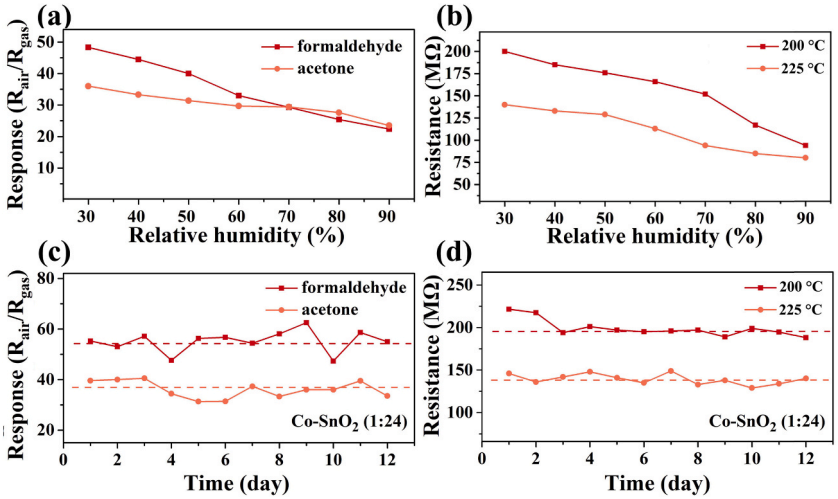

Fig. 5. The responses (a) and the baseline resistances (b) of the 3D IO Co-SnO_2 (1:24 atom%) MF-based sensor at different humidity (30–90% RH); The long-term stability measurement of response (c) and resistance (d) of the 3D IO Co-SnO_2 (1:24 atom%) MF-based sensor toward 100 ppm formaldehyde at 200 °C and 100 ppm acetone at 225 °C.

sensor to have high resistance. (ii) At step two, when detecting formaldehyde, acetone (Eqs. (5 and 6)), and other reducing gases, the reducing gas reacts with the chemisorbed oxygen, and electrons are released from the oxygen to the semiconductor conduction band, leading to the increase of the electron concentration, the decrease of the depletion layer thickness, and the decline of the barrier height.

$$HCHO + 2O^- \leftrightarrow CO_2 + H_2O + 2e^- \quad (5)$$

$$CH_3COCH_3 + 8O^- \leftrightarrow 3CO_2 + 3H_2O + 8e^- \quad (6)$$

In this research, the excellent gas sensing properties could be attributed to the following aspects. For molecular dynamics, the Knudsen diffusion formula explains that gas sensing properties are related to the microstructure of the sensing materials [38]. It is worth mentioning that the 3D IO macroporous structure is a reliable framework for gas sensing. 3D IO structured materials with good permeability and porosity, as well as a large specific area and pore volume that can promote the diffusion of gas molecules. As shown in Fig. S7, the N_2 adsorption/desorption isotherms of the 3D IO pure SnO_2 and Co-SnO_2 (1:24 atom%) MFs all exhibited a type of III isotherm. The specific surface area of the 3D IO Co-SnO_2 (1:24 atom%) and pure SnO_2 MFs were 53.6 and 51.6 $m^2\ g^{-1}$, respectively, which were all much higher than that of the SnO_2 solid nanospheres (~10.7 $m^2\ g^{-1}$). The doping macroporous material had a pore diameter of ~138 nm and the pure material was ~140 nm, coincident with the SEM/TEM analysis. Therefore, it could be concluded that the Co-doping had barely any influence on the morphology. Additionally, the macroporous structure was conducive to the effective diffusion of the gas molecules and helpful for improving the utilization efficiency of the sensing materials, indicating that the materials had better gas sensing properties. In addition, the in-situ Co-doping had a significant impact on the gas sensing response. The doping of the Co^{2+} and Co^{3+} for the Sn^{4+} could generate more oxygen vacancies, thus leading to the increase of the chemisorbed oxygen [39]. The defect reaction Eqs. (7–9) was

$$Co_3O_4 \rightarrow CoO + Co_2O_3, \quad (7)$$

$$CoO \rightarrow Co'_{Sn} + V_o^{\cdot} + O_O^X, \quad (8)$$

$$Co_2O_3 \rightarrow 2Co^{\cdot}_{Sn} + V_o^{\cdot\cdot} + 3O_O^X. \quad (9)$$

To verify that the electron transfer could be obviously influenced by doping, the Fermi level (E_f) and the maximum valence band (E_v) of the SnO_2 and Co-SnO_2 (1:24 atom%) MFs were obtained with UPS (Fig. 6(a and b)). The work function could be obtained as shown in Eq. (10):

$$W_F = h\nu - E_{cut-off\ (\text{high binding energy})}, \quad (10)$$

where hν (~21.22 eV) is the energy of the UV lamp. The Fermi levels of the SnO_2 and Co-SnO_2 (1:24 atom%) MFs were calculated to be − 3.08 eV and − 2.70 eV, respectively. Moreover, the E_V was determined by defining the cut-off values of the high binding energy and the low binding energy. Thus, the corresponding E_V levels were − 5.43 eV for the pure SnO_2 MFs and − 5.80 eV for the Co-SnO_2 (1:24 atom%) MFs [40]. The calculated results showed that the work function of the Co-SnO_2 (1:24 atom%) decreased, indicating the elevation of the Fermi level after doping. As is well known, when the SMO gas sensor was exposed in air, the oxygen molecules were adsorbed on the surface of the sensing materials and they captured electrons from the semiconductor conduction band, forming the surface chemisorbed oxygen. The energy band bent upward until the Fermi level became the same as the LUMO of the chemisorbed oxygen. Therefore, as shown in Fig. 6(c), the elevation of the Fermi level increased the depletion layer thickness and led to a larger energy level between the SMO and chemisorbed oxygen, finally resulting in the increase of the chemisorbed oxygen, which was beneficial for improving the gas sensing performance. Accordingly, the higher gas sensitivity of the 3D IO Co-SnO_2 (1:24 atom%) compared with the pure SnO_2 was attributed to the increase of the chemisorbed oxygen generated by the elevation of the Fermi level, which meant that more chemisorbed oxygen participated in the surface sensing reaction while detecting target gas molecules after cobalt doping.

In addition, gas sensing performance is also associated with the band gap of SMO sensing materials [41]. For example, if the SMO has a narrower band gap, the potential energy barrier will decrease and the carrier concentration change will be not obvious while forming the depletion layer [42]. Accordingly, it is necessary to control the doping concentration to optimize the band gap. As shown in Fig. 7(a and b) and Fig. S8, the band gaps of the 3D IO SnO_2 and Co-SnO_2 (Co/Sn = 1:16,

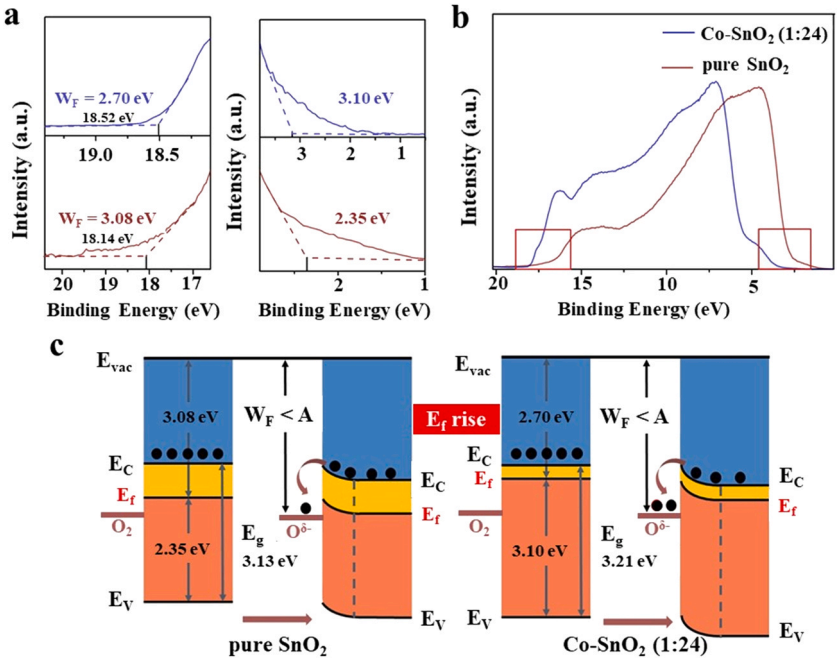

Fig. 6. (a and b) The UPS spectra of the 3D IO SnO_2 and Co-SnO_2 (1:24 atom%) MF sensing materials. (c) The energy band structure of the sensing materials.

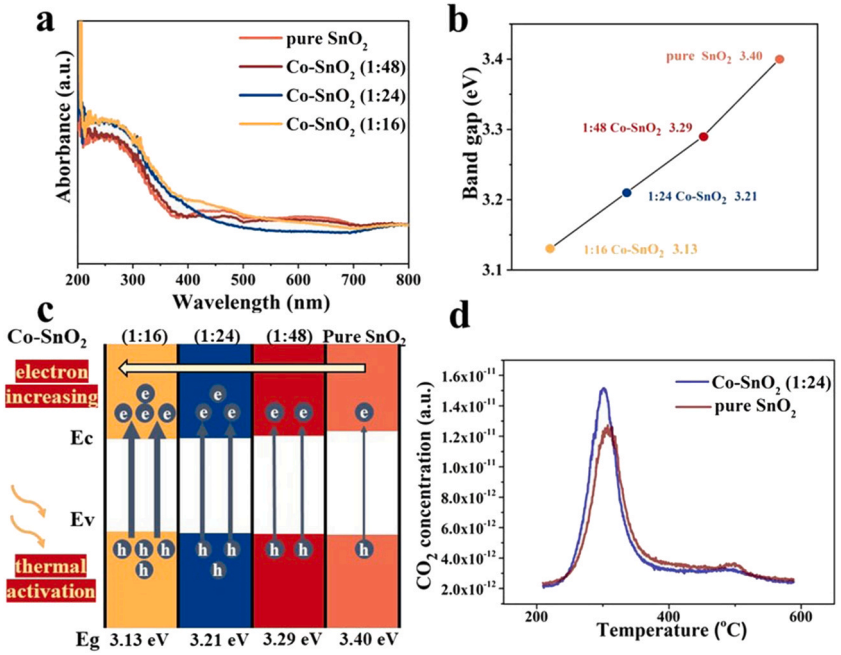

Fig. 7. (a) The UV visible absorption spectrogram of the 3D IO SnO_2 and Co-SnO_2 (Co/Sn = 1:16, 1:24, 1:48 atom%) MF sensing materials. (b) The calculation of the band gap energy using a Tauc-Plot analysis. (c) Schematic energy diagram illustrating the effect of the Co doping sensing materials. (d) The HCHO-TPR of 3D IO SnO_2 and Co-SnO_2 (1:24 atom%) MF sensing materials.

1:24, and 1:48 atom%) MF sensing materials were 3.40 eV, 3.13 eV, 3.21 eV, and 3.29 eV. Additionally, the UV visible absorption spectra could be modified when an additional energy level such as the oxygen vacancy was introduced into the band gap of sensing materials (Fig. 7 (a)) [43]. With the increasing Co doping concentration, the band gap of the Co-SnO_2 became smaller and the 3D IO Co-SnO_2 (1:24 atom%) sensing material with the band gap of 3.21 eV possessed the best gas sensing performance. More importantly, the HCHO-TPR was also used to characterize the concentration of chemisorbed oxygen of pure SnO_2 and Co-SnO_2 (1:24 atom%) and to simulate the gas sensing reaction. The experimental procedure is described in Fig. S9. As shown in Fig. 7(d), the generated concentration of CO_2 could reflect the intensity of the sensing reaction between the HCHO and the chemisorbed oxygen. More HCHO was consumed for the Co-SnO_2 compared with pure SnO_2 for the same condition, further verifying that the cobalt doping could produce more oxygen vacancy and surface active sites and lead to the generation of more chemisorbed oxygen bound to the sensing material surfaces [23]. Thus, it could be concluded that more chemisorbed oxygen would participate in the sensing reaction on a heteroion doped SMO surface while being exposed to the target VOC.

4. Conclusions

In summary, the 3D IO Co-SnO_2 MF sensing materials were designed and prepared with ultrasonic nebulizing deposition (UND) combined with the self-assembly polystyrene sphere template. The 3D IO MF structure could achieve effective gas diffusion and enhance gas accessibility to improve the utilization efficiency of the sensing material. Importantly, the doping of cobalt could elevate the Fermi level position, decrease the band gap, induce vacancy defects, and increase the surface chemisorbed oxygen, finally resulting in the enhancement of the sensing performance to formaldehyde and acetone. Accordingly, the 3D IO Co-SnO_2 (1:24 atom%) MF-based sensor exhibited ultra-sensitivity, a fast response, and high selectivity to the low concentration of formaldehyde (at 200 °C) and acetone (at 225 °C), respectively. Thus, a single gas sensor based on ordered porous Co-SnO_2 multilayer films with dual functionality could achieve the synchronous, sensitive, and selective detection of two different VOC gases (formaldehyde and acetone) via the tuning of the operating temperature.

CRediT authorship contribution statement

Ke Chen, Conceptualization, Investigation, Formal analysis, Methodology, Data curation, Writing – original draft, Writing – review & editing. **Yue Zhou**, Formal analysis. **Rongrong Jin**, Formal analysis. **Tianshuang Wang**, Conceptualization, Methodology, Supervision, Writing – review & editing. **Fangmeng Liu**, Supervision. **Chenguang Wang**, Supervision. **Xu Yan**, Supervision.**Peng Sun**, Conceptualization, Methodology, Supervision, Writing – review & editing. **Geyu Lu,** Funding acquisition.

Declaration of Competing Interest

The authors declare that they have no known competing financial interests or personal relationships that could have appeared to influence the work reported in this paper.

Acknowledgments

This work is supported by the National Nature Science Foundation of China (Grant Number 61833006 and 61831011). Jilin Province Science and Technology Development Plan Program (No. 20200301010RQ). The National Postdoctoral Program for Innovative Talents (Grant Number BX20200149). Scientific Research Project of the Education Department of Jilin Province (Grant No. JJKH20211090KJ).

Conflict of Interest

The authors declare no competing financial interest.

Appendix A. Supporting information

Supplementary data associated with this article can be found in the online version at doi:10.1016/j.snb.2021.130807.

References

[1] T. Salthammer, S. Mentese, R. Marutzky, Formaldehyde in the indoor environment, Chem. Rev. 110 (2010) 2536–2572.
[2] A. Songur, O.A. Ozen, M. Sarsilmaz, The toxic effects of formaldehyde on the nervous system, Rev. Environ. Contam. Toxicol. 203 (2010) 105–118.
[3] J.H. Arts, J. Mojet, L.J. van Gemert, H.H. Emmen, J.H. Lammers, J. Marquart, R. A. Woutersen, V.J. Feron, An analysis of human response to the irritancy of acetone vapors, Crit. Rev. Toxicol. 32 (2002) 43–66.
[4] T. Wang, Z. Huang, Z. Yu, B. Wang, H. Wang, P. Sun, H. Suo, Y. Gao, Y. Sun, T. Li, G. Lu, Low operating temperature toluene sensor based on novel α-Fe_2O_3/SnO_2 heterostructure nanowire arrays, RSC Adv. 6 (2016) 52604–52610.
[5] C.S. Moon, H.-R. Kim, G. Auchterlonie, J. Drennan, J.-H. Lee, Highly sensitive and fast responding CO sensor using SnO_2 nanosheets, Sens. Actuators B Chem. 131 (2008) 556–564.
[6] J.-H. Lee, Gas sensors using hierarchical and hollow oxide nanostructures: overview, Sens. Actuators B Chem. 140 (2009) 319–336.
[7] K.R. Phillips, T. Shirman, E. Shirman, A.V. Shneidman, T.M. Kay, J. Aizenberg, Nanocrystalline precursors for the co-assembly of crack-free metal oxide inverse opals, Adv. Mater. 30 (2018), 1706329.
[8] D. McNulty, V. Landgraf, S. Trabesinger, Simplifying the synthesis of carbon inverse opals, RSC Adv. 10 (2020) 24108–24114.
[9] X. Zhou, J. Liu, C. Wang, P. Sun, X. Hu, X. Li, K. Shimanoe, N. Yamazoe, G. Lu, Highly sensitive acetone gas sensor based on porous $ZnFe_2O_4$ nanospheres, Sens. Actuators B Chem. 206 (2015) 577–583.
[10] N. Vogel, M. Retsch, C.A. Fustin, A. Del Campo, U. Jonas, Advances in colloidal assembly: the design of structure and hierarchy in two and three dimensions, Chem. Rev. 115 (2015) 6265–6311.
[11] T. Wang, S. Zhang, Q. Yu, X. Kou, P. Sun, F. Liu, H. Lu, X. Yan, G. Lu, 3D inverse opal nanostructured multilayer films of two-component heterostructure composites: a new-generation synthetic route and potential application as high-performance acetone detector, Sens. Actuators B Chem. 276 (2018) 262–270.
[12] H. Gao, Q. Yu, S. Zhang, T. Wang, P. Sun, H. Lu, F. Liu, X. Yan, F. Liu, X. Liang, Y. Gao, G. Lu, Nanosheet-assembled NiO microspheres modified by Sn^{2+} ions isovalent interstitial doping for xylene gas sensors, Sens. Actuators B Chem. 269 (2018) 210–222.
[13] M. D'Arienzo, L. Armelao, A. Cacciamani, C.M. Mari, S. Polizzi, R. Ruffo, R. Scotti, A. Testino, L. Wahba, F. Morazzoni, One-step preparation of SnO_2 and Pt-doped SnO_2 as inverse opal thin films for gas sensing, Chem. Mater. 22 (2010) 4083–4089.
[14] X. Kou, F. Meng, K. Chen, T. Wang, P. Sun, F. Liu, X. Yan, Y. Sun, F. Liu, K. Shimanoe, G. Lu, High-performance acetone gas sensor based on Ru-doped SnO_2 nanofibers, Sens. Actuators B: Chem. 320 (2020), 128292.
[15] V. Saasa, T. Malwela, Y. Lemmer, M. Beukes, B. Mwakikunga, The hierarchical nanostructured Co-doped WO_3/carbon and their improved acetone sensing perfomance, Mater. Sci. Semicond. Process. 117 (2020), 105157.
[16] T. Wang, B. Jiang, Q. Yu, X. Kou, P. Sun, F. Liu, H. Lu, X. Yan, G. Lu, Realizing the control of electronic energy level structure and gas-sensing selectivity over heteroatom-doped In_2O_3 spheres with an inverse opal microstructure, ACS Appl. Mater. Interfaces 11 (2019) 9600–9611.
[17] T. Wang, S. Zhang, Q. Yu, S. Wang, P. Sun, H. Lu, F. Liu, X. Yan, G. Lu, Novel self-assembly route assisted ultra-fast trace volatile organic compounds gas sensing based on three-dimensional opal microspheres composites for diabetes diagnosis, ACS Appl. Mater. Interfaces 10 (2018) 32913–32921.
[18] F. Gu, H. Wang, D. Han, Z. Wang, Enhancing the sensing performance of SnO_2 inverse opal thin films by In and Au doping, Sens. Actuators B Chem. 245 (2017) 1023–1031.
[19] N. Gil-Gonzalez, F. Benito-Lopez, E. Castano, M.C. Morant-Minana, Imidazole-based ionogel as room temperature benzene and formaldehyde sensor, Mikrochim Acta 187 (2020) 638.
[20] H. Gao, Q. Yu, K. Chen, P. Sun, F. Liu, X. Yan, F. Liu, G. Lu, Ultrasensitive gas sensor based on hollow tungsten trioxide-nickel oxide (WO_3-NiO) nanoflowers for fast and selective xylene detection, J. Colloid Interface Sci. 535 (2019) 458–468.
[21] W. Guo, S.G. Surya, V. Babar, F. Ming, S. Sharma, H.N. Alshareef, U. Schwingenschlögl, K.N. Salama, Selective toluene detection with Mo_2CT_x MXene at room temperature, ACS Appl. Mater. Interfaces 12 (2020) 57218–57227.
[22] K. Hwang, J. Ahn, I. Cho, K. Kang, K. Kim, J. Choi, K. Polychronopoulou, I. Park, Microporous elastomer filter coated with metal organic frameworks for improved selectivity and stability of metal oxide gas sensors, ACS Appl. Mater. Interfaces 12 (2020) 13338–13347.
[23] Y. Yu, E. Wu, Y. Chen, Z. Feng, S. Zheng, H. Zhang, W. Pang, J. Liu, D. Zhang, Volatile organic compounds discrimination based on dual mode detection, Nanotechnology 29 (2018), 245502.
[24] G. Li, Z. Cheng, Q. Xiang, L. Yan, X. Wang, J. Xu, Bimetal PdAu decorated SnO_2 nanosheets based gas sensor with temperature-dependent dual selectivity for detecting formaldehyde and acetone, Sens. Actuators B Chem. 283 (2019) 590–601.
[25] C. Wang, X. Cui, J. Liu, X. Zhou, X. Cheng, P. Sun, X. Hu, X. Li, J. Zheng, G. Lu, Design of superior ethanol gas sensor based on Al-doped NiO nanorod-flowers, ACS Sens. 1 (2016) 131–136.
[26] Y. Ma, Y. Ma, G. Giuli, T. Diemant, R.J. Behm, D. Geiger, et al., Conversion/alloying lithium-ion anodes-enhancing the energy density by transition metal doping, Sustain. Energy Fuels 2 (2018) 2601–2608.
[27] C. Xu, J. Tamaki, N. Miura, N. Yamazoe, Grain size effects on gas sensitivity of porous SnO_2-based elements, Sens. Actuators B Chem. 3 (1991) 147–155.
[28] J. Guo, Y. Li, B. Jiang, H. Gao, T. Wang, P. Sun, F. Liu, X. Yan, X. Liang, Y. Gao, J. Zhao, G. Lu, Xylene gas sensing properties of hydrothermal synthesized SnO_2-Co_3O_4 microstructure, Sens. Actuators B: Chem. 310 (2020), 127780.
[29] T.-H. Kim, S.-Y. Jeong, Y.K. Moon, J.-H. Lee, Dual-mode gas sensor for ultrasensitive and highly selective detection of xylene and toluene using Nb-doped NiO hollow spheres, Sens. Actuators B: Chem. 301 (2019), 127140.
[30] H. Gao, D. Wei, P. Lin, C. Liu, P. Sun, K. Shimanoe, N. Yamazoe, G. Lu, The design of excellent xylene gas sensor using Sn-doped NiO hierarchical nanostructure, Sens. Actuators B Chem. 253 (2017) 1152–1162.
[31] T. Hyodo, H. Inoue, H. Motomura, K. Matsuo, T. Hashishin, J. Tamaki, Y. Shimizu, M. Egashira, NO_2 sensing properties of macroporous In_2O_3-based powders fabricated by utilizing ultrasonic spray pyrolysis employing polymethylmethacrylate microspheres as a template, Sens. Actuators B Chem. 151 (2010) 265–273.
[32] J.C. Traeger, Heat of formation for the formyl cation by photoionization mass spectrometry, Int J. Mass Spectrom. 66 (1985) 271–282.
[33] H. Chen, J. Hu, G.-D. Li, Q. Gao, C. Wei, X. Zou, Porous Ga-In bimetallic oxide nanofibers with controllable structures for ultrasensitive and selective detection of formaldehyde, ACS Appl. Mater. Interfaces 9 (2017) 4692–4700.
[34] Z. Wen, L. Tian-mo, Gas-sensing properties of SnO_2-TiO_2-based sensor for volatile organic compound gas and its sensing mechanism, Phys. B Condens. Matter 405 (2010) 1345–1348.
[35] D. Meng, D. Liu, G. Wang, Y. Shen, X. San, M. Li, F. Meng, Low-temperature formaldehyde gas sensors based on NiO-SnO_2 heterojunction microflowers assembled by thin porous nanosheets, Sens. Actuators B Chem. 273 (2018) 418–428.
[36] M.E. Franke, T.J. Koplin, U. Simon, Metal and metal oxide nanoparticles in chemiresistors: does the nanoscale matter? Small 2 (2006) 36–50.
[37] N. Barsan, M. Schweizer-Berberich, W. Göpel†, Fundamental and practical aspects in the design of nanoscaled SnO_2 gas sensors: a status report, Fresenius, J. Anal. Chem. 365 (1999) 287–304.
[38] N. Yamazoe, G. Sakai, K. Shimanoe, Oxide semiconductor gas sensors, Catal. Surv. Asia 7 (2003) 63–75.
[39] M.A. Ponce, R. Parra, M.S. Castro, C.M. Aldao, Conductance analysis of (Co, Nb, Fe)-doped SnO_2 thick film gas sensors, J. Mater. Sci. Mater. Electron. 18 (2007) 1171–1177.
[40] K. Liu, K.S. Ganesh, J. Nie, Z. He, C. Xia, W. Dong, X. Wang, H. Wang, B. Wang, Characterizing the blocking electron ability of the Schottky junction in SnO_2-SDC semiconductor-ionic membrane fuel cells, ACS Sustain. Chem. Eng. 8 (2020) 10357–10368.
[41] J. Wang, R. Chen, L. Xiang, S. Komarneni, Synthesis, properties and applications of ZnO nanomaterials with oxygen vacancies: a review, Ceram. Int. 44 (2018) 7357–7377.
[42] T. Wang, Q. Yu, S. Zhang, X. Kou, P. Sun, G. Lu, Rational design of 3D inverse opal heterogeneous composite microspheres as excellent visible-light-induced NO_2 sensors at room temperature, Nanoscale 10 (2018) 4841–4851.
[43] M. Al-Hashem, S. Akbar, P. Morris, Role of oxygen vacancies in nanostructured metal-oxide gas sensors: a review, Sens. Actuators B: Chem. 301 (2019), 126845.

Ke Chen received her BS degree from the Electronic Science and Engineering department, Jilin University, China in 2019. Presently, she is a graduate student and interested in the synthesis and characterization of the semiconducting functional materials and gas sensors.

Yue Zhou received her BE degree from the Electronic Science and Engineering department, Jilin University, China in 2020. Now, she is a graduate student and interested in the synthesis and characterization of the semiconducting functional materials and gas sensors.

Rongrong Jin received his BE degree from the Electronic and Information Engineering department, Changchun Science and Engineering University, China in 2020. Now, he is a graduate student and interested in the synthesis and characterization of the semiconducting functional materials and gas sensors.

Tianshuang Wang received his Ph.D. degree from Jilin University in 2020. He is now a Postdoctoral Fellow at State Key Laboratory of Inorganic Synthesis and Preparative Chemistry, Jilin University. His research focuses on the development of porous structure metal oxide and multi-functional zeolite catalysts for chemical sensor application.

Fangmeng Liu received his Ph.D. degree in 2017 from College of Electronic Science and Engineering, Jilin University, China. Now he is a lecturer at Jilin University, China. His current research interests include the application of functional materials and development of solid state electrolyte gas sensor and flexible device.

Chenguang Wang received his PhD degree from the College of Chemistry, Jilin University in 2013. He then joined the Institute of Transformative Bio-Molecules, Nagoya University as a postdoctoral fellow. In 2019, he joined the College of Electronic Science and Engineering, Jilin University as a professor. His research interests focus on the design and synthesis of organic fluorescent molecules and their applications in fluorescence bioimaging.

Xu Yan received his M.S. degree in 2013 from Nanjing Agricultural University. He joined the group of Prof. Xingguang Su at Jilin University and received his Ph.D. degree in June 2017. Since then, he did postdoctoral work with Prof. Geyu Lu. Currently, his research

interests mainly focus on the development of functional nanomaterials for chem/bio sensors.

Peng Sun received his Ph.D. degree from Jilin University, in 2014. He was appointed the lecturer in Jilin University in the same year. Now, he is engaged in the synthesis and characterization of the semiconducting functional materials and gas sensors.

Geyu Lu received his M.S. degree from Jilin University in 1988 and Ph.D. degree from Kyushu University in 1998. Now he is a full professor of Jilin University. His current research interests include the development of chemical sensors and the application of the function materials.